

Haem oxygenase is synthetically lethal with the tumour suppressor fumarate hydratase

Christian Frezza¹, Liang Zheng¹, Ori Folger², Kartik N. Rajagopalan³, Elaine D. MacKenzie¹, Livnat Jerby², Massimo Micaroni⁴, Barbara Chaneton¹, Julie Adam⁵, Ann Hedley¹, Gabriela Kalna¹, Ian P. M. Tomlinson⁶, Patrick J. Pollard⁵, Dave G. Watson⁷, Ralph J. Deberardinis³, Tomer Shlomi^{8*}, Eytan Ruppin^{2,9*} & Eyal Gottlieb¹

Fumarate hydratase (FH) is an enzyme of the tricarboxylic acid cycle (TCA cycle) that catalyses the hydration of fumarate into malate. Germline mutations of *FH* are responsible for hereditary leiomyomatosis and renal-cell cancer (HLRCC)¹. It has previously been demonstrated that the absence of *FH* leads to the accumulation of fumarate, which activates hypoxia-inducible factors (HIFs) at normal oxygen tensions^{2–4}. However, so far no mechanism that explains the ability of cells to survive without a functional TCA cycle has been provided. Here we use newly characterized genetically modified kidney mouse cells in which *Fh1* has been deleted, and apply a newly developed computer model of the metabolism of these cells to predict and experimentally validate a linear metabolic pathway beginning with glutamine uptake and ending with bilirubin excretion from *Fh1*-deficient cells. This pathway, which involves the biosynthesis and degradation of haem, enables *Fh1*-deficient cells to use the accumulated TCA cycle metabolites and permits partial mitochondrial NADH production. We predicted and confirmed that targeting this pathway would render *Fh1*-deficient cells non-viable, while sparing wild-type *Fh1*-containing cells. This work goes beyond identifying a metabolic pathway that is induced in *Fh1*-deficient cells to demonstrate that inhibition of haem oxygenation is synthetically lethal when combined with *Fh1* deficiency, providing a new potential target for treating HLRCC patients.

To study metabolic adaptation of *FH*-deficient cells we first generated immortalized kidney cells from mice homozygous for a conditionally targeted *Fh1* allele³. These cells contain LoxP sites flanking exons 3 and 4 (*Fh1*^{fl/fl}) (Fig. 1a and Supplementary Fig. 2a) and express normal levels of Fh1 protein (Fig. 1b). To generate *Fh1*^{-/-} cells the *Fh1*^{fl/fl} cells were infected with recombinant adenovirus expressing Cre recombinase and two clones (CL1 and CL19) were selected from the infected pools. Both clones were genetically confirmed to contain homozygous *Fh1*-deleted (knockout) alleles (Fig. 1a) and did not express Fh1 protein (Fig. 1b).

To assess the biochemical consequences of *Fh1* deletion on TCA cycle function, the intracellular levels of several TCA cycle metabolites were measured by gas chromatography–mass spectrometry (GC–MS) (Fig. 1c). *Fh1*^{-/-} cells accumulate substantial amounts of fumarate, which reached levels more than a 100-fold that of *Fh1*^{fl/fl} cells. In addition, a sevenfold increase in succinate levels and a marked decrease of malate and citrate were detected (Fig. 1d). In cancer cells, the TCA cycle is largely supplied through the metabolism of glucose and glutamine⁵. To investigate the effects of *Fh1* deletion on carbon supply to the TCA cycle, cells were cultured in medium containing ¹³C-labelled glucose and unlabelled glutamine, or vice versa, and ¹³C-enrichment of fumarate and succinate was analysed. When ¹³C-glucose was used, the

majority of fumarate was unlabelled (m+0), indicating that glucose is a minor source of carbon for the TCA cycle in both *Fh1*^{fl/fl} and *Fh1*^{-/-} cells (Fig. 1e). On the other hand, when cells were incubated with ¹³C-glutamine most of the fumarate was labelled (Fig. 1f). In *Fh1*^{-/-} cells cultured with uniformly labelled glutamine (Fig. 1f), the vast majority of the labelled fumarate contained all four carbon atoms derived from glutamine (m+4). By contrast, in *Fh1*^{fl/fl} cells, the fumarate pool contained substantial fractions of molecules with fewer than four ¹³C atoms due to processing of fumarate beyond the Fh1 step. The lack of these products in *Fh1*^{-/-} cells confirms that no accessory pathway exists in these cells to circumvent the loss of Fh1 enzymatic activity, indicating a true blockade of the cycle. Notably, the ¹³C-enrichment profiles of

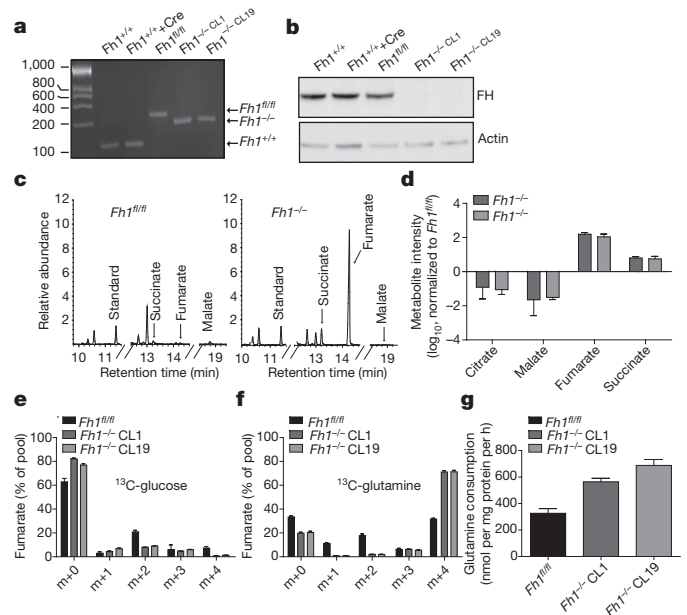


Figure 1 | Characterization of *Fh1*-deficient cells. **a**, PCR analysis of genomic DNA of epithelial kidney cells of the indicated genotype. Numbers indicate base pairs. **b**, Fh1 protein levels of the indicated cells were detected by western blot analysis. **c**, Representative chromatogram of a GC–MS analysis performed from the indicated cell lines. Annotated metabolites are indicated by the arrows. **d**, Fold change of the indicated TCA cycle metabolites in *Fh1*^{-/-} compared to control *Fh1*^{fl/fl} cells ($n = 3$). **e**, **f**, Isotopomer distribution of intracellular fumarate. Cells were incubated with either ¹³C-glucose (**e**) or ¹³C-glutamine (**f**) and fumarate isotopomers (with the indicated mass shift) were analysed ($n = 3$). **g**, Glutamine consumption rate of the indicated cell lines ($n = 3$). All data are presented as mean \pm s.e.m.

¹Cancer Research UK, Beatson Institute for Cancer Research, Switchback Road, Glasgow G61 1BD, UK. ²The Blavatnik School of Computer Science, Tel Aviv University, Tel Aviv 69978, Israel. ³Department of Pediatrics and McDermott Center for Human Growth and Development, University of Texas–Southwestern Medical Center at Dallas, 5323 Harry Hines Blvd, Dallas, Texas 75390-9063, USA. ⁴The University of Queensland, Institute for Molecular Bioscience, St Lucia, Brisbane, Queensland 4072, Australia. ⁵Henry Wellcome Building for Molecular Physiology, University of Oxford, Roosevelt Drive, Oxford OX3 7BN, UK. ⁶Molecular and Population Genetics Laboratory, Wellcome Trust Centre for Human Genetics, University of Oxford, Oxford OX3 7BN, UK. ⁷Strathclyde Institute of Pharmaceutical and Biomedical Sciences, University of Strathclyde, 27 Taylor Street, Glasgow G4 0NR, UK. ⁸Computer Science Department, Technion, Israel Institute of Technology, Haifa, 32000, Israel. ⁹The Sackler School of Medicine, Tel Aviv University, Tel Aviv 69978, Israel.

*These authors contributed equally to this work.

succinate perfectly matched fumarate results, underlining the presence of a flux of carbons from glutamine to fumarate via succinate. In addition, no reverse flux of TCA cycle metabolites was detected (Supplementary Fig. 2b, c). (See Supplementary Fig. 1 for a diagram summarizing these results.) Consistent with the increased contribution of glutamine to the pool of TCA cycle intermediates, *Fh1*^{-/-} cells used significantly more glutamine than *Fh1*^{fl/fl} cells (Fig. 1g).

Because the TCA cycle is a major source for mitochondrial NADH, the truncation of the TCA cycle may have severe bioenergetic outcomes. Indeed, steady-state levels of mitochondrial NADH in *Fh1*^{-/-} cells were lower than those of control cells (Fig. 2a; untreated and Supplementary Fig. 2d for quantification). However, *Fh1*^{-/-} cells still generate significant amounts of NADH and retained normal mitochondrial membrane potential (Fig. 2a). In addition, depolarizing the mitochondria by using the protonophore carbonyl cyanide *m*-chlorophenyl hydrazone (CCCP) decreased mitochondrial NADH, whereas blocking NADH oxidation with rotenone, an inhibitor of NADH:ubiquinone oxidoreductase, increased mitochondrial NADH in both control and *Fh1*-deficient cells. These results indicate that despite having a truncated TCA cycle, *Fh1*-deficient cells retain significant mitochondrial bioenergetic activity and are capable of generating and oxidizing NADH. Because NADH oxidation in the mitochondria fuels the respiratory chain, the oxygen consumption rate was analysed. *Fh1*^{-/-} cells showed a significant reduction of their cyanide-dependent respiratory rate (Fig. 2b) when compared to wild-type cells. The decrease in respiration was not due to a general reduction in mitochondrial number as was assessed both microscopically (Fig. 2a) and by mitochondrial DNA quantification (Supplementary Fig. 2e). Furthermore, and as was recently reported for HLRCC (Online Mendelian Inheritance in Man accession number 605839) patient-derived cells⁶, although mitochondria of *Fh1*^{-/-} cells appear larger under electron microscopy they do retain some organized cristae structures (Supplementary Fig. 2f). The

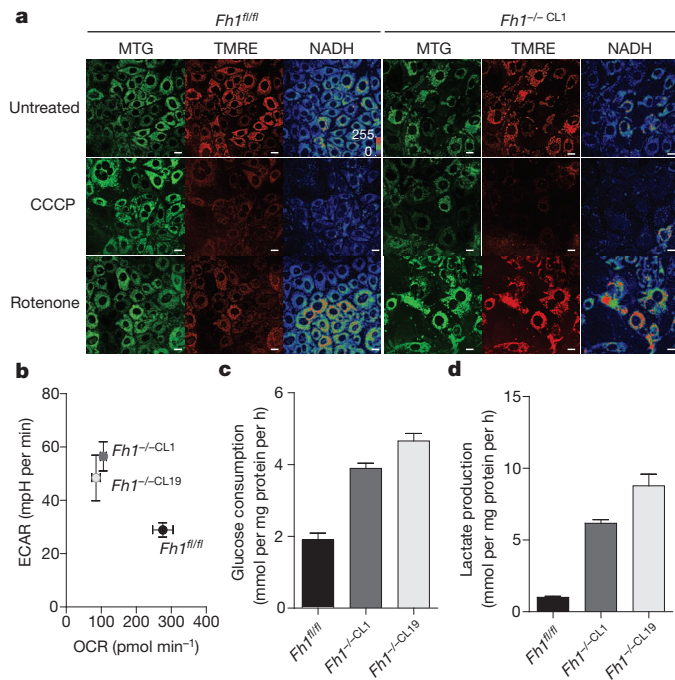


Figure 2 | Metabolic analyses of *Fh1*^{-/-} cells. **a**, Confocal microscopy was used to assess mitochondrial membrane potential and mitochondrial NADH levels in the indicated cell lines. Where indicated, cells were incubated with rotenone or CCCP before visualization. Scale bar: 50 μ m. MTG, MitoTracker green; TMRE, tetramethyl rhodamine ethyl ester. **b**, Representative graph of oxygen consumption rate (OCR) versus extracellular acidification rate (ECAR). Data are presented as mean \pm s.d. ($n = 6$). **c**, **d**, Glucose consumption (**c**) and lactate production (**d**) of the indicated cell lines. Data are presented as mean \pm s.e.m. ($n = 3$).

decrease in respiration of *Fh1*^{-/-} cells was associated with an increase in glycolysis as indicated initially by the increased extracellular acidification rate (Fig. 2b) and further confirmed by the increase in glucose consumption and lactate production (Fig. 2c, d).

Metabolic networks are highly interconnected, making them resistant to most single gene perturbations⁷. To elucidate the metabolic changes that enable the survival of *Fh1*^{-/-} cells despite having a truncated TCA cycle, we took a systemic approach based on flux balance analysis (FBA) to obtain a genome-scale model of cellular metabolism, as very commonly used in modelling of microbial metabolism⁸. We adopted an *in silico* modelling approach for cancer metabolism⁹ (see Supplementary Information for details) to predict genes for which elimination together with *Fh1* would selectively affect the growth ability of *Fh1*^{-/-} cells without affecting the wild-type *Fh1*^{fl/fl} cells (predicted to be synthetic lethal with *Fh1*). This modelling involved the reconstruction of genome-scale metabolic network models of the metabolism of *Fh1*^{fl/fl} and *Fh1*^{-/-} cells, using a generic computational method for building metabolic models of specific human tissues¹⁰. The reconstruction of the models began with the identification of core sets of metabolic-enzyme-coding genes that are expressed in *Fh1*^{fl/fl} and *Fh1*^{-/-} cells, based on accompanying microarray gene expression analysis (Supplementary Fig. 3), added to a set of metabolic genes that are highly expressed across many cancer cell lines¹¹. Then, for each cell line, a minimal, consistent metabolic network that includes the corresponding core reactions set was extracted from an existing generic human model¹², such that each of the core reactions can potentially carry a stoichiometrically balanced metabolic flux (Supplementary Table 1). As conventionally done in FBA modelling¹³, cellular growth requirements are modelled via the addition of a growth reaction, which represents the steady-state consumption of essential biomass constituents required for cellular proliferation, based on previous knowledge of their relative concentrations. The resulting metabolic models were used to predict the consequences of gene knock-outs based on their effect on reducing biomass production rate, considering the rate of glucose, glutamine and oxygen uptake as well as lactate secretion measured in each of the cell lines (Supplementary Table 2).

Overall, 24 reactions were predicted by this analysis to be synthetic lethal with *Fh1*, as their deletion is predicted to affect growth only in the *Fh1*^{-/-} metabolic network model (Fig. 3a and Supplementary Table 3). Of these, 18 belong to a linear pathway of haem metabolism, which was also predicted by the model to have increased flux in *Fh1*^{-/-} cells. Haem biosynthesis is a cataplerotic pathway that uses TCA-cycle-derived carbon to generate haem, whereas the haem degradation pathway generates bilirubin that can be removed from the cells. Thus, haem biosynthesis and degradation would generate a linear pathway starting with glutamine uptake and ending with bilirubin excretion. This biochemical escape valve would allow some generation of mitochondrial NADH (Supplementary Fig. 1). Interestingly, the transcriptomic analysis revealed that three of the predicted synthetic lethal genes were also upregulated in *Fh1*^{-/-} cells (Fig. 3b): haem oxygenase 1 (*Hmox1*; but not *Hmox2*), which catabolizes haem to biliverdin; biliverdin reductase B (*Bilvrb*), which catabolises biliverdin to bilirubin; and UDP-glucuronyl transferase 2b34 (*Ugt2b34*), which facilitates bilirubin excretion. The expression levels of these genes were validated (Fig. 3c, d) and the increase in *Hmox1* protein levels was also confirmed (Fig. 3e). None of these transcriptional changes could be simply attributed to the expression of Cre recombinase, because they were not observed in the Cre-infected *Fh1*^{+/+} cells, which do not express the conditional (LoxP) *Fh1* alleles (Fig. 3c, d). Notably, although these three genes exhibit significantly increased expression in *Fh1*^{-/-} cells, the potential role of this metabolic pathway in the survival of the *Fh1*-deficient cells could not have been predicted solely by its gene expression response to *Fh1* knockout, as many additional pathways show a similar increase in expression (Supplementary Fig. 3b).

To validate the activation of the haem pathway in *Fh1*^{-/-} cells, as predicted by the FBA model, we measured the levels of excreted bilirubin in the media using liquid chromatography–mass spectrometry

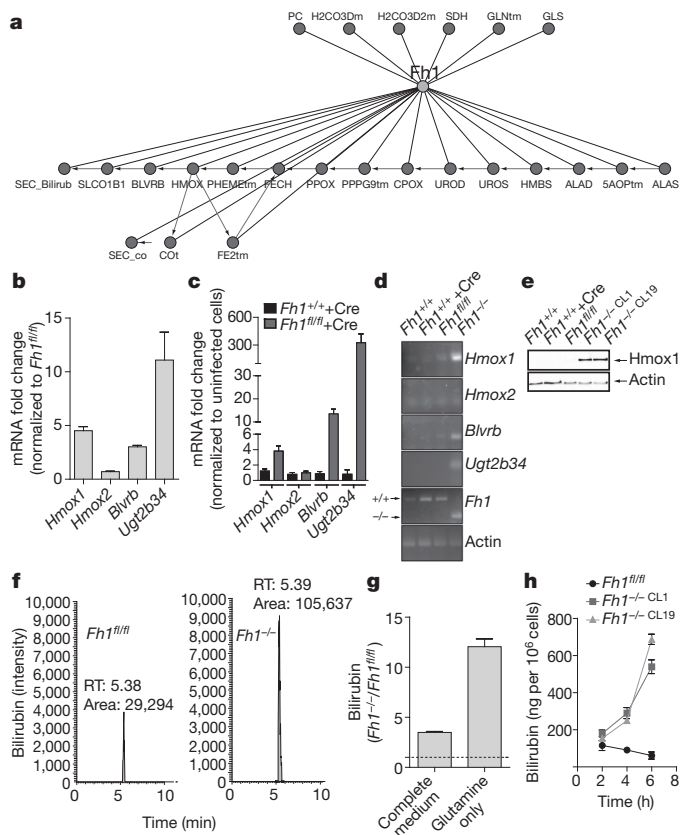


Figure 3 | The haem pathway is predicted to be synthetically lethal with *Fh1*.

a, Synthetic lethal pairs with *FH* were predicted using the FBA metabolic modelling. The haem synthesis and degradation pathway (bottom) was highly represented. 5AOPtm, aminolevulinic acid (ALA) transport; ALAD, ALA dehydratase; ALAS, ALA synthase; BLVRB, biliverdin reductase; COt, carbon monoxide (CO) transport; CPOX, coproporphyrinogen oxidase; FE2tm, iron transport; FECH, ferrochelatase; GLNtm, glutamine transport; GLS, glutaminase; H2CO3Dm/D2m, carbonate transport; HMBS, hydroxymethylbilane synthase; HMOX, haem oxygenase; PC, pyruvate carboxylase; PHEMETm, haem transporter; PPOX, protoporphyrinogen oxidase; PPPG9tm, porphyrin transporter; SDH, succinate dehydrogenase; SEC_Bilirub, bilirubin excretion; SEC_co, CO excretion; SLCO1B1, bilirubin transporter; UROD, uroporphyrinogen (URO) decarboxylase; UROS, URO synthase. **b**, Transcriptomic analysis of *Fh1*^{-/-} cells revealed an increased expression of three genes involved with the haem degradation pathway: *Hmox1*, *Blvrb* and UDP-glucuronyl transferase 2b34 (*Ugt2b34*). Data are presented as mean \pm s.d. ($n = 2$). **c**, **d**, The expression levels of the genes indicated in **b** were verified using qPCR (**c**) and end-point RT-PCR (**d**). Data are presented as mean \pm s.e.m. ($n = 3$). **e**, *Hmox1* protein levels in the indicated cell lines were detected by western blot analysis. **f**, Representative LC-MS chromatogram of bilirubin excreted by the indicated cell lines after 24 h in complete medium. RT, retention time (min); area is expressed as arbitrary units and was calculated by the integration of the bilirubin peak. **g**, Analysis of bilirubin excretion from the indicated cell lines grown either in complete medium or in the absence of glucose for 6 h. Data are presented as mean \pm s.e.m. ($n = 3$). **h**, Kinetics of bilirubin excretion from the indicated cell lines incubated in glucose-free medium. Data are presented as mean \pm s.d. ($n = 2$).

(LC-MS) (Fig. 3f). In agreement with our model, the levels of excreted bilirubin were higher in *Fh1*-deficient cells (Fig. 3f-h). Importantly, excretion of bilirubin in *Fh1*^{-/-} cells was further increased when cells were transiently deprived of glucose (Fig. 3g), underpinning their increased dependency on glutamine as a mitochondrial carbon source during glucose deprivation.

In support of these findings, analysis of a published transcriptomic data set of human uterine fibroids¹⁴ revealed significant upregulation of *HMOX1* (but not *HMOX2*) in *FH*-mutant fibroids (Supplementary Fig. 4). These results prompted us to validate the predicted synthetic

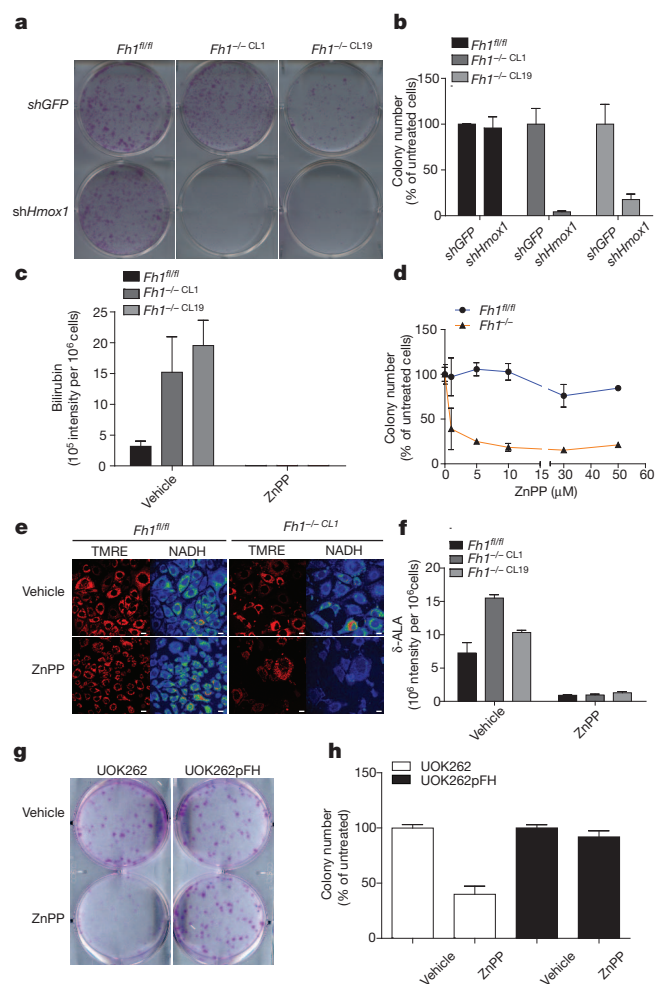


Figure 4 | Targeting the haem degradation pathway is lethal for *Fh1*-deficient cells. **a**, Representative images of a colony assay of cells infected with lentiviruses expressing either a non-targeting shRNA sequence (*shGFP*) or with an shRNA targeting *Hmox1*. **b**, Quantification of the clonogenic assay described in **a**. **c**, Quantification of bilirubin excretion before and after treatment with $10 \mu\text{mol l}^{-1}$ ZnPP for 24 h. **d**, Clonogenic survival assay of wild-type or *Fh1*-deficient cells treated with the indicated concentration of ZnPP. **e**, The effect of ZnPP (treated as in **c**) on mitochondrial NADH was analysed microscopically. **f**, The effect of ZnPP (treated as in **c**) on intracellular ALA levels was measured by LC-MS. **g**, **h**, Representative images (**g**) and colony quantification (**h**) of a clonogenic survival assay of UOK262 and UOK262pFH cells treated with $1 \mu\text{mol l}^{-1}$ ZnPP for 4 days. All the data are presented as mean \pm s.e.m., ($n = 3$).

lethality between *Fh1* and *Hmox1* in our mouse kidney cell model. First, *Hmox1* was efficiently silenced by lentiviral infection of short hairpin (sh)RNAs (*shHmox1* 1-3) (Supplementary Fig. 5a). All three shRNAs demonstrated significant reduction in growth of *Fh1*-deficient cells, whereas there was minimal to no effect on the control cells (Supplementary Fig. 5b). The effect of the most efficient shRNA (*shHmox1* 1) on long-term colony survival was further studied and it resulted in a marked decrease in colony number in *Fh1*^{-/-} cells but not in wild-type cells (Fig. 4a, b). Importantly, the surviving *shHmox1*-infected *Fh1*^{-/-} cells escaped silencing and their *Hmox1* expression levels reverted to that of mock-infected cells (Supplementary Fig. 5c).

For further confirmation of the above findings, we used zinc protoporphyrin (ZnPP), a *Hmox* inhibitor¹⁵. First, the efficacy of *Hmox* inhibition by ZnPP was tested by measuring bilirubin excretion. In both wild-type and *Fh1*-deficient cells bilirubin excretion was completely blocked by ZnPP (Fig. 4c). Whereas acute treatment with ZnPP had no profound effect on wild-type cells, it decreased the growth of *Fh1*^{-/-} cells (Supplementary Fig. 5d). More importantly, similarly to

Hmox1 silencing, long-term treatment with ZnPP abolished colony formation of *Fh1*^{-/-} cells but had very little effect on wild-type cells (Fig. 4d). Furthermore, treatment of *Fh1*-deficient cells with ZnPP resulted in a decrease in mitochondrial NADH, whereas only slight changes were observed in control cells (Fig. 4e). These observations further elucidate the bioenergetic support that the glutamine–bilirubin linear pathway provides to *Fh1*-deficient cells.

δ-Aminolevulinic acid (ALA) synthase (ALAS), the entry point and rate-limiting step of haem biosynthesis (Supplementary Fig. 1), is tightly (negatively) controlled by haem and protoporphyrin to prevent the accumulation of porphyrins and its toxic consequences (porphyria)¹⁶. Therefore, it is likely that by blocking haem degradation, ZnPP can also inhibit the activity of ALAS. Indeed, the intracellular levels of ALA were decreased in ZnPP-treated cells (Fig. 4f), indicating that ZnPP has profound effects on the entire haem pathway beyond the inhibition of *Hmox*. To confirm further the importance of the cataplerotic role of haem biosynthesis in supporting *Fh1*-deficient cells, we also inhibited ALAS using hemin, an approved drug used for acute porphyria¹⁷. Similarly to *Hmox* inhibition, the inhibition of ALAS had no effect on control cells, whereas *Fh1*-deficient cells were sensitive to hemin treatment (Supplementary Fig. 5e).

Finally, to extend our findings to a human model of *FH* deficiency, we studied the recently described HLRCC-derived renal cancer cell line UOK262 (ref. 6). These cells are pseudo-hypoxic due to the accumulation of fumarate¹⁸. UOK262 cells were reintroduced with V5-tagged FH protein which was correctly localized to the mitochondria, improved oxygen consumption and restored low levels of fumarate (Supplementary Fig. 6a–c). Importantly, restoring TCA function to the *FH*-deficient UOK262 cells also markedly reduced bilirubin secretion and rendered the cells less sensitive to the HMOX and ALAS inhibitors ZnPP and hemin, respectively (Fig. 4g, h and Supplementary Fig. 6d, e). Importantly, the sensitivity of the *FH*-deficient UOK262 cells to ZnPP is independent on HIF activity (Supplementary Fig. 6f–h).

Taken together, the results of this work demonstrate that the inhibition of the haem biosynthesis/degradation pathway in general, and *Hmox* in particular, is synthetically lethal with *Fh1* both in mouse and in human cell lines. Hence, its inhibition would provide a valid therapeutic window for the treatment of HLRCC patients as it would specifically target *FH*-deficient cells while sparing normal tissues, thus reducing nonspecific toxic effects.

METHODS SUMMARY

Epithelial kidney cells were obtained from *Fh1*^{fl/fl} mice following the method described previously¹⁹. The *Fh1*^{-/-} cell line was generated by infection with AhCRE adenoviral particles. The genotype was assessed by PCR on genomic DNA using the primers described in the Methods. TCA metabolites and their isotopomer enrichment analyses were performed by GC–MS after incubating the cells with either U-¹³C-glucose or U-¹³C-glutamine. Mitochondrial potential and NADH were analysed by confocal microscopy using the potentiometric probe TMRE and NADH autofluorescence, respectively. Glucose and glutamine consumption and lactate secretion were measured using the BioProfile Basic4 Analyser. Oxygen consumption rate and extracellular acidification rate were measured using the Seahorse XF24. Expression levels of the genes in the haem pathway were determined by qPCR and validated using semi-quantitative RT–PCR as detailed in the Methods. Bilirubin, ALA, citrate and aconitate levels were measured by LC–MS. Sulphorhodamine B was used to stain colonies. Colonies were counted using ImageJ software.

Full Methods and any associated references are available in the online version of the paper at www.nature.com/nature.

Received 13 July 2010; accepted 11 July 2011.

Published online 17 August 2011.

- Tomlinson, I. P. *et al.* Germline mutations in *FH* predispose to dominantly inherited uterine fibroids, skin leiomyomata and papillary renal cell cancer. *Nature Genet.* **30**, 406–410 (2002).

- Isaacs, J. S. *et al.* HIF overexpression correlates with biallelic loss of fumarate hydratase in renal cancer: novel role of fumarate in regulation of HIF stability. *Cancer Cell* **8**, 143–153 (2005).
- Pollard, P. J. *et al.* Targeted inactivation of *fh1* causes proliferative renal cyst development and activation of the hypoxia pathway. *Cancer Cell* **11**, 311–319 (2007).
- Frezza, C., Pollard, P. J. & Gottlieb, E. Inborn and acquired metabolic defects in cancer. *J. Mol. Med.* **89**, 213–220 (2011).
- DeBerardinis, R. J. *et al.* Beyond aerobic glycolysis: transformed cells can engage in glutamine metabolism that exceeds the requirement for protein and nucleotide synthesis. *Proc. Natl Acad. Sci. USA* **104**, 19345–19350 (2007).
- Yang, Y. *et al.* UOK 262 cell line, fumarate hydratase deficient (*FH*^{-/-}/*FH*^{fl/fl}) hereditary leiomyomatosis renal cell carcinoma: *in vitro* and *in vivo* model of an aberrant energy metabolic pathway in human cancer. *Cancer Genet. Cytogenet.* **196**, 45–55 (2010).
- Deutscher, D., Meilijson, I., Kupiec, M. & Ruppin, E. Multiple knockout analysis of genetic robustness in the yeast metabolic network. *Nature Genet.* **38**, 993–998 (2006).
- Price, N. D., Papin, J. A., Schilling, C. H. & Palsson, B. O. Genome-scale microbial *in silico* models: the constraints-based approach. *Trends Biotechnol.* **21**, 162–169 (2003).
- Folger, O. *et al.* Predicting selective drug targets in cancer through metabolic networks. *Mol. Syst. Biol.* **7**, 501 (2011).
- Jerby, L., Shlomi, T. & Ruppin, E. Computational reconstruction of tissue-specific metabolic models: application to human liver metabolism. *Mol. Syst. Biol.* **6**, 401 (2010).
- Lee, J. K. *et al.* A strategy for predicting the chemosensitivity of human cancers and its application to drug discovery. *Proc. Natl Acad. Sci. USA* **104**, 13086–13091 (2007).
- Duarte, N. C. *et al.* Global reconstruction of the human metabolic network based on genomic and bibliomic data. *Proc. Natl Acad. Sci. USA* **104**, 1777–1782 (2007).
- Orth, J. D., Thiele, I. & Palsson, B. O. What is flux balance analysis? *Nature Biotechnol.* **28**, 245–248 (2010).
- Vanharanta, S. *et al.* Distinct expression profile in fumarate-hydratase-deficient uterine fibroids. *Hum. Mol. Genet.* **15**, 97–103 (2006).
- Labbe, R. F., Vreman, H. J. & Stevenson, D. K. Zinc protoporphyrin: A metabolite with a mission. *Clin. Chem.* **45**, 2060–2072 (1999).
- Schoenfeld, N. *et al.* The effects of metalloporphyrins, porphyrins and metals on the activity of delta-aminolevulinic acid synthase in monolayers of chick embryo liver cells. *Biochem. Pharmacol.* **33**, 2783–2788 (1984).
- Anderson, K. E. & Collins, S. Open-label study of hemin for acute porphyria: clinical practice implications. *Am. J. Med.* **119**, e19–24 (2006).
- Sudarshan, S. *et al.* Fumarate hydratase deficiency in renal cancer induces glycolytic addiction and hypoxia-inducible transcription factor 1 α stabilization by glucose-dependent generation of reactive oxygen species. *Mol. Cell. Biol.* **29**, 4080–4090 (2009).
- Mathew, R., Degenhardt, K., Haramaty, L., Karp, C. M. & White, E. Immortalized mouse epithelial cell models to study the role of apoptosis in cancer. *Methods Enzymol.* **446**, 77–106 (2008).

Supplementary Information is linked to the online version of the paper at www.nature.com/nature.

Acknowledgements This work was supported by Cancer Research UK. We would like to acknowledge the Patterson Institute for Cancer Research for the Exon Array analysis. C.F. is supported by an EMBO long term fellowship (ALTF330). P.J.P. is in receipt of a Beit Memorial Fellowship funded by the Wellcome Trust (WT091112MA). D.G.W. and L.Z. would like to acknowledge SULSA (Scottish Universities Life Science Alliance). R.J.D. and K.N.R. are supported by the NIH (DK072565-05) and the Cancer Prevention and Research Institute of Texas (HIRP100437-01). O.F., T.S. and E.R. are supported by the Israel Science Foundation (ISF) and the Israel Cancer Research Foundation. L.J. is supported by the Edmond J. Safra Bioinformatics program at TAU. We thank UOB Tumor Cell Line Repository and W. Marston Linehan for providing us with the UOK262 cell lines, and A. King for editorial work.

Author Contributions C.F. and E.G. conceived the project, analysed the data and wrote the manuscript. C.F. and E.D.M. generated the kidney cell lines. O.F., L.J., T.S. and E.R. built the metabolic network of the cells and predicted the synthetic lethal genes. J.A., I.P.M.T. and P.J.P. provided the *Fh1*^{fl/fl} mice, generated the UOKpFH cell line and provided genotyping tools. G.K. and A.H. performed the bioinformatics and statistical analysis. L.Z. and D.G.W. performed the LC–MS analysis. K.N.R. and R.J.D. performed GC–MS and the BioProfile metabolic analyses. C.F. performed all other experiments with the help of B.C. M.M. performed the electron microscopy. All the authors discussed the results and commented on the manuscript.

Author Information Microarray data are deposited at the website <http://bioinformatics.picr.man.ac.uk/vice/Welcome.vice>, accession reference GE_EG(2). Reprints and permissions information is available at www.nature.com/reprints. The authors declare no competing financial interests. Readers are welcome to comment on the online version of this article at www.nature.com/nature. Correspondence and requests for materials should be addressed to E.G. (egottlieb@beatson.gla.ac.uk).

METHODS

Cell culture: *Fh1^{fl/fl}* and *Fh1^{-/-}* cell lines. Epithelial kidney cells were obtained from *Fh1^{fl/fl}* mice following the method described previously¹⁹. 2×10^5 cells were either left untreated or infected with Cre recombinase-encoding adenovirus (Ad5CMVCRE) using 300 p.f.u. per cell. After 4 days of infection, 100 cells were plated and grown onto 15-cm dishes. Individual colonies were harvested using paper cloning discs (Sigma) and transferred onto 24-well plates for clonal expansion. Cells were grown using DMEM (21969-035, Invitrogen) supplemented with 10% FBS, 2 mmol l⁻¹ glutamine, 1 mmol l⁻¹ pyruvate and 50 μ g l⁻¹ uridine. UOK262 were cultured in DMEM (21969-035, Invitrogen) supplemented with 10% FBS, 2 mmol l⁻¹ glutamine, 1 mmol l⁻¹ pyruvate.

UOK262 and UOKpFH cell lines. UOK262 cells were grown using high glucose DMEM (Invitrogen) supplemented with 2 mM glutamine and 10% FBS. Full-length FH human cDNA was cloned into pEF1-V5-HIS. Transfected cells were selected in 1 mg ml⁻¹ G418 and single clones were expanded. Expression and subcellular localization of FH was confirmed by immunofluorescence using anti V5 antibody with a FITC-conjugated secondary antibody; mitochondria were stained using Mitotraker red and nuclei were stained with DAPI.

Genomic DNA, mitochondrial DNA, RNA isolation and qPCR analyses. 2×10^5 cells were harvested in RLT buffer (Qiagen) using a cell lifter and lysates were passed through QiaShredder columns (Qiagen). Genomic DNA and mRNA were then separated using the AllPrep micro kit (Qiagen) following manufacturer's instructions. Quantification of RNA was obtained on the Eppendorf Biophotometer using Eppendorf single-sealed cuvettes, UVette (Eppendorf UK Limited).

Genomic DNA was assessed to determine the different genotypes of the different cell lines using the primers F1, F3 and R1 described above. The PCR of the genomic DNA was performed using GoTaq DNA polymerase (Promega) and 0.5 μ M primers following the manufacturer's instructions. The PCR program was: 15 min at 95 °C followed by 40 cycles of 45 s at 95 °C, 30 s at 55 °C and then 30 s at 72 °C. The PCR products were separated in a 2% agarose gel stained with ethidium bromide.

Mitochondrial DNA content was analysed from the genomic DNA extraction by comparing the expression levels of a nuclear-encoded single-copy gene, amyloid precursor protein (APP), to the DNA levels of the mtDNA encoded cytochrome *c* oxidase subunit II (COXII), as performed previously²⁰. The following primers were used: APP: FW 5'-GGCTGCTGGCAGAACCCAG-3', RV 5'-CCCTGACGG GTCTGACTCCCA-3'; COXII FW 5'-AACTGATGCCATCCAGGCCGA-3', RV 5'-GGTGAAGGTGCCAGTGGGAATGT-3'.

For PCR analyses, 1 μ g of mRNA was retro-transcribed into cDNA using M-Mulv Reverse Transcriptase and random hexamers and qPCR reactions were performed using a Sybr-green master mix as per the manufacturer's instructions (Dynamo qPCR kit, Finnzymes, ThermoScientific). In brief, 0.5 μ M primers, ROX dye, and a 1 μ l of a 1:10 dilution of cDNA in a final volume of 20 μ l were used. The primers were designed by the Roche Universal Library (UPL, Roche, <http://www.roche-applied-science.com/sis/rtqcr/upl/ezhome.html>) and the sequences are indicated in Supplementary Table 5. Real-time PCR was performed on the 7500 Fast Real-Time PCR System (Life Technologies Corporation) and expression levels of the indicated genes were calculated using the $\Delta\Delta C_t$ method by the appropriate function of the software using actin as calibrator. The results were further validated using Polg2R as calibrator (data not shown). The PCR programme was: 15 min at 95 °C followed by 40 cycles of 10 s at 94 °C, 30 s at 55 °C and then 30 s at 72 °C. A final extension at 72 °C for 10 min was allowed before the melting curve, which was used to confirm the presence of single PCR products. For the semi-quantitative end-point RT-PCR the cDNA prepared as indicated above was cycled for 25 times and the PCR products were separated using a 2% agarose gel stained with ethidium bromide.

Exon array analysis. RNA obtained as described above was subjected to a Microarray analysis using a GeneChip Mouse Exon 1.0 ST Array (Affimetrix). The .Cel files were normalized and analysed in Partek Genomics Suite Software, version 6.5beta Copyright 2010. Interrogating and control core probe sets were imported and default RMA setting used, including quantile normalization, log₂ transformation and mean probe-set summarization. In gene-level analysis the multiway analysis of variance (ANOVA) was used to identify significantly regulated genes from one of the experimental groups and linear contrasts performed between all pairs of experimental conditions. Multiple test corrections were performed for all calculated *P*-values. Step-up *P*-value, a *P*-value that controls the false discovery rate, and the fold change values were used for further selection of significantly differentially expressed genes.

Microarray bioinformatics analysis. Affimetrix Human Genome U133A .Cel files of 15 wild-type and 7 mutant fumarate hydratase samples were normalized and analysed in Partek Genomics Suite Software, version 6.5 Copyright 2010.

RMA normalization and log₂ transformation of the data was followed by *t*-test and multiple test corrections of *P*-values.

Immunoblotting. 2×10^5 cells were lysed in RIPA buffer (150 mM sodium chloride, 1.0% NP-40, 0.5% sodium deoxycholate, and 50 mM Tris, pH 8.0) supplemented with a 1:100 dilution of the protein inhibitor cocktail (Sigma). Protein concentration was determined using the Bicinchoninic Acid Assay (ThermoScientific) using BSA as standard. Equal amounts of protein were loaded into 4–12% Tris-Mops pre-casted gels (Invitrogen) and electrophoretically separated using MOPS running buffer (Invitrogen). After SDS-PAGE, proteins were blotted onto 0.22 μ m nitrocellulose (Millipore) and probed with the following antibodies, all at 1:1,000 dilution in 5% non-fat milk: Fh1 (polyclonal rabbit AutogenBioclar NE054 /7S), Hmox1 (polyclonal rabbit SPA-896, Stressgen Enzo Life Science), actin (mouse monoclonal AC-40; Sigma). Membranes were then incubated with secondary HRP-conjugated antibodies at 1:1,000 dilution in 5% non-fat milk: anti-mouse (7076) and anti rabbit (7074), both from Cell Signaling Technology. ECL (RPN 2209, GE Healthcare UK) was used for chemiluminescence detection. For Hmox1 and actin western blot, a secondary donkey anti-rabbit (926 32213, Licor) and donkey anti-mouse (926 32212, Licor) IR800 at 1:1,000 dilution were used. The IR scanning was performed using the Licor Odyssey scanner (channel, 800; brightness, 50; contrast, 50; sensitivity, auto; resolution, 169.492 μ m; pixel area, 0.02873 mm²; intensity, 5) and acquired using Odyssey software version 3.

Measurement of NADH and mitochondrial potential. 2×10^5 cells were grown in 3.5-cm glass-bottom dishes (MatTek corporation) and loaded with 50 nmol l⁻¹ MitoTracker green (MTG; Invitrogen) and 10 nmol l⁻¹ tetramethyl rhodamine ethyl ester (TMRE) (Invitrogen) for 30 min at 37 °C. Cells were then left untreated or treated as indicated. The final concentrations and incubation time of the drugs are: 5 μ mol l⁻¹ rotenone, 5 min; 10 μ mol l⁻¹ carbonylcyanide-*m*-chlorophenyl hydrazone (CCCP) for 1 min. Images were collected with a Leica TCS SP2 AOBs inverted laser scanning microscope equipped with a Coherent 351–364 nm UV laser using a 63 \times /1.32.ph3 oil HCX PL APO objective, resolution 1,024 \times 1,024 d.p.i., 8-bit image depth, 200 Hz scanning speed, and line average 2. The acquisition of the two-colour images was performed in a sequential scanning mode to minimize spectral bleed-through artefacts. Laser excitation was 364 nm for NADH autofluorescence, 488 nm for MTG and 568 nm for TMRE, whereas fluorescence emission was adjusted with AOBs at 390–486 nm for NADH, 501–546 nm for MTG and 580–620 nm for TMRE. To increase sensitivity of NADH detection, the pinhole aperture used for all channels was set at 2.62 airy units. The images were quantified for NADH levels using the Image Pro Plus software (Media Cybernetics) using MTG signal as a mask to outline the mitochondrial reticulum. Intensity of fluorescence of NADH determined in the outlined areas was then normalized to MTG fluorescence intensity. To better appreciate changes in NADH fluorescence intensity, a rainbow look-up table was applied to the relevant images using the appropriate function of ImageJ (ImageJ, US National Institutes of Health, <http://rsb.info.nih.gov/ij/>).

Measurement of glucose, lactate and glutamine. 2×10^5 cells were plated onto 6-cm dishes and cultured until 90% confluent. Each dish was then replenished with fresh medium and cultured for 16 h. After the culture period, the medium was recovered for determination of glucose, lactate and glutamine concentration using a BioProfile Basic4 Analyser (NOVA Biomedical) and compared to concentration of these metabolites in the starting medium. To correct for spontaneous glutamine degradation, an additional dish with no cells was cultured in parallel. Raw values of glutamine and glucose utilization, and lactate secretion, were converted to rates by correcting for the protein content at the end of the assay, and the duration of the assay in hours.

Measurement of OCR and ECAR rate. 2×10^4 *Fh1^{fl/fl}* cells, 3×10^4 *Fh1^{-/-}*, or 3×10^4 UOK262 and UOK262pFH cells were plated onto XF24 plates (Seahorse Bioscience) and incubated at 37 °C, 5% CO₂ for 24 h. The medium was then replaced with 675 μ l of unbuffered assay media (Seahorse Bioscience) supplemented with 2 mmol l⁻¹ glutamine, 25 mmol l⁻¹ glucose and 2% FBS (pH was adjusted to 7.4 using sodium hydroxide 0.5 M) and cells were then placed at 37 °C in a CO₂-free incubator. Basal oxygen consumption rate (OCR) and extracellular acidification rate (ECAR) were then recorded using the XF24 plate reader. At the end of the experiment 1 mmol l⁻¹ potassium cyanide or 1 μ mol l⁻¹ antimycin A were added to measure mitochondria-independent oxygen consumption. Each cycle of measurement consisted of 3 min mixing, 3 min waiting and 4 min measuring. OCR and ECAR were normalized to cell number calculated at the end of the experiments. To obtain the mitochondrial-dependent OCR, only the cyanide-sensitive respiration was used. Homogeneous plating of the cells and cell count were assessed by fixing the cells with trichloroacetic acid 10% for 1 h at 4 °C and then staining the fixed cells with 0.47% solution of sulphorhodamine B (SRB) (Sigma).

Determination of TCA cycle metabolites and isotopomer enrichment analysis by GC-MS. Cells were cultured in DMEM supplemented with 10% FBS, 2 mmol

l^{-1} sodium pyruvate, $50 \mu\text{g ml}^{-1}$ uridine, $100 \text{ units ml}^{-1}$ penicillin and $100 \mu\text{g ml}^{-1}$ streptomycin in 6-cm tissue culture dishes. Metabolic experiments were performed when cells were approximately 90% confluent. Medium for ^{13}C glucose labelling experiments contained $10 \text{ mM D-[U-}^{13}\text{C]-glucose}$ (Cambridge Isotope Labs) and 4 mmol l^{-1} unlabelled glutamine. Medium for ^{13}C -glutamine labelling experiments contained 10 mmol l^{-1} unlabelled glucose and 4 mmol l^{-1} L-[U- ^{13}C]-glutamine (Isotec). Medium containing ^{13}C -labelled nutrients did not contain sodium pyruvate. Each dish of cells was rinsed in phosphate-buffered saline, and replenished with the labelling medium. After 16 h, cells were rinsed with normal saline, and metabolites were extracted in $0.5 \text{ ml } 50\% \text{ MeOH}$ pre-chilled to -20°C . 100 nmol of sodium oxobutyrate was added as a standard to the extracted metabolites. Extracts were concentrated under blown air and derivatized using Tri-Sil trimethylsilane reagent (Thermo Scientific). One microlitre of each derivatized sample was injected onto an Agilent 6980N GC coupled to an Agilent 5973N mass selective detector. GC-MS data were analysed using MSDChem Data Analysis Software (Agilent). Retention times of the sodium oxobutyrate standard, succinate, fumarate and malate were 11.4, 13.2, 14.2 and 18.7 min, respectively. Informative ions were monitored for derivatized, unenriched oxobutyrate (m/z 230), succinate (247), fumarate (245), and malate (335). Relative metabolite abundances were determined by normalizing abundances of each metabolite to the internal standard and to protein content. For mass isotopomer analysis, the abundance of each mass isotopomer ($m+0$, $m+1$, ... $m+n$, where n is the number of carbons in the parent metabolite) was corrected for natural ^{13}C abundance using published methods²¹.

Measurement of bilirubin, ALA, lactate and TCA cycle intermediates by LC-MS. 1×10^6 cells were plated onto 10-cm dishes and cultured in standard medium for 12 h. The medium was replaced by fresh standard medium or by medium without glucose or without glutamine for the indicated time. Fresh medium in the same dishes but without cells was incubated simultaneously and used as a reference. $100 \mu\text{l}$ of medium were diluted into $200 \mu\text{l}$ of acetonitrile (Fisher). The solution was centrifuged at $16,000g$ for 4 min at 4°C . The supernatant was collected and transferred into autosampler vials for LC-MS determinations. Cells were lysed with a solution kept in dry ice/methanol (-80°C) composed of 50% methanol and 30% acetonitrile in water and quickly scraped. The insoluble material was immediately pelleted in a cooled centrifuge (0°C) and the supernatant was collected for subsequent LC-MS analysis. A ZIC-HILIC column ($4.6 \text{ mm} \times 150 \text{ mm}$, guard column $2.1 \text{ mm} \times 20 \text{ mm}$, Merck) was used for LC separation using formic acid, water acetonitrile as component of the mobile phase.

Measurement of ^{13}C -labelled metabolites by LC-MS. 1×10^6 cells were plated onto 10-cm dishes and cultured in standard medium for 12 h. The medium was replaced by fresh medium supplemented with $2 \text{ mM U-}^{13}\text{C}$ -glutamine for the indicated time. Fresh medium in the same dishes but without cells was incubated simultaneously and used as a reference. Cells were then lysed with a solution kept in dry ice/methanol (-80°C) composed of 50% methanol and 30% acetonitrile in water and quickly scraped. The insoluble material was immediately pelleted in a cooled centrifuge at $16,000g$ for 15 min at 0°C and the supernatant was collected for subsequent LC-MS analysis. The amount of extraction solution was calculated according to the number of cells present in the sample dish, extrapolated using a 'counter dish' cultured in the same conditions of the sample dishes. A concentration of $1 \text{ ml per } 2 \times 10^6$ cells was used in the extraction solutions. Intermediates were separated using a liquid chromatography system.

Colony formation assay. Clonogenic survival assay was performed as previously described²² with minor modifications. The plating efficiency among different cell lines was different therefore $100 \text{ Fh1}^{\text{fl/fl}}$ cells and $600 \text{ Fh1}^{-/-}$ cells per each 10-cm dish were plated, whereas 150 UOK262 cells, 150 UOK262pFH cells and 600

$\text{UOK262 shHIF}\beta$ cells per each 6-well plate were plated. Twenty-four hours after plating, cells were treated with the indicated doses of ZnPP, $100 \mu\text{mol l}^{-1}$ hemin (Sigma) or vehicle (DMSO for ZnPP or water for the other drug). UOK262 cells infected with shHIF1 β plasmid were selected with $2 \mu\text{g ml}^{-1}$ puromycin. Hemin was prepared by dissolving the drug in a solution of 0.2 M sodium carbonate, pH 10. The pH was then adjusted at 7.4 and the mixture was sterilized using $0.45 \mu\text{m}$ filters. The final concentration of the solution was determined using the molar extinction coefficient of hemin at $\lambda_{407 \text{ nm}}$ $\epsilon = 36,000 \text{ M cm}^{-1}$ (ref. 23). The medium was changed every 2 days for a total of 7 days treatment for murine cell lines and a total of 4 days of treatment for human cell lines. The medium was then replaced with fresh standard medium without drug or vehicle and cells were left to grow for 2–4 more days. The cells were then fixed as described²⁴ by adding ice-cold trichloroacetic acid onto the plate at the final concentration of 3% for 1 h at 4°C . Cells were then washed with water and air-dried. Cells were then stained using 0.47% SRB for 30 min at room temperature. SRB was removed and cells were thoroughly washed with 1% acetic acid and air-dried. Plates were scanned at the resolution of 600 d.p.i., 24-bit saved as TIFF files and analysed using the object count function of the ImageJ software.

ShRNA of Hmox1. The lentiviral shRNA plasmids against *Hmox1* (NM_010442) and the non-targeted shGFP, and a scramble sequence were all purchased from Open Biosystems, TRC1 library (Thermoscientific). The three independent shRNAs were identified as follows: 1, TRCN0000071578; 2, TRCN0000071579; 3, TRCN0000071580 and the sequences are shown in Supplementary Table 6. The viral supernatant was obtained from the filtered growth media of the packaging cells HEK293T transfected with appropriate packaging plasmids and either shRNA for *Hmox1* or control pLKO plasmids, using calcium phosphate procedure. $2 \times 10^5 \text{ Fh1}^{\text{fl/fl}}$, $\text{Fh1}^{-/-}$ and UOK262 cells were then plated on 6-well plates and infected with the viral supernatant prepared as indicated above. After 2 days, the medium was replaced by selection medium containing $4 \mu\text{g ml}^{-1}$ puromycin. Cells were then allowed to grow under selection for 2 days and then an equal number of cells was plated onto 6-well plates and grown using the selection media. After a week cells were fixed using SRB following the procedure described above.

shRNA of HIF1 β (ARNT). 2×10^5 cells were infected with shRNA for *HIF1 β* (NM_001668.2) and control plasmid using lentiviral infection. HEK293T and relevant packaging plasmids were used to produce the lentiviral suspension. shRNA plasmids were purchased from Openbiosystems and the clone number TRCN0000003819 (for the sequence see Supplementary Table 6) was used for subsequent infections. After infection, cells were selected using $4 \mu\text{g ml}^{-1}$ puromycin.

Statistical analyses. The data (mean \pm s.e.m.) are representative of 3–5 independent experiments, performed in technical triplicates if not differently indicated. Data were analysed and presented with Graphpad Prism 5.01 software (GraphPad Software Inc.).

- Malena, A., Loro, E., Di Re, M., Holt, I. J. & Vergani, L. Inhibition of mitochondrial fission favours mutant over wild-type mitochondrial DNA. *Hum. Mol. Genet.* **18**, 3407–3416 (2009).
- Fernandez, C. A., Des Rosiers, C., Previs, S. F., David, F. & Brunengraber, H. Correction of ^{13}C mass isotopomer distributions for natural stable isotope abundance. *J. Mass Spectrom.* **31**, 255–262 (1996).
- Franken, N. A., Rodermond, H. M., Stap, J., Haveman, J. & van Bree, C. Clonogenic assay of cells *in vitro*. *Nature Protocols* **1**, 2315–2319 (2006).
- Uc, A., Stokes, J. B. & Britigan, B. E. Heme transport exhibits polarity in Caco-2 cells: evidence for an active and membrane protein-mediated process. *Am. J. Physiol. Gastrointest. Liver Physiol.* **287**, G1150–G1157 (2004).
- Vichai, V. & Kirtikara, K. Sulforhodamine B colorimetric assay for cytotoxicity screening. *Nature Protocols* **1**, 1112–1116 (2006).